

# Effect of the precursor chemistry on the crystallization of triple cation mixed halide perovskites

Mriganka Singh<sup>1†</sup>, Maged Abdelsamie<sup>2†</sup>, Qihua Li<sup>3</sup>, Tim Kodalle<sup>1,4</sup>, Do-Kyoung Lee<sup>1,5</sup>, Simon Arnold<sup>6</sup>, Davide R. Ceratti<sup>7,8</sup>, Jonathan L. Slack<sup>4</sup>, Craig P. Schwartz<sup>5</sup>, Christoph J. Brabec<sup>6</sup>, Shuxia Tao<sup>3</sup>, Carolin M. Sutter-Fella<sup>1\*</sup>

<sup>1</sup>*Molecular Foundry Division, Lawrence Berkeley National Laboratory, 1 Cyclotron Road, Berkeley CA 94710, USA*

<sup>2</sup>*Interdisciplinary Research Center for Intelligent Manufacturing and Robotics, Materials Science and Engineering Department, King Fahd University of Petroleum and Minerals, Dhahran 31261, Saudi Arabia*

<sup>3</sup>*Materials Simulation and Modelling, Department of Applied Physics, Eindhoven University of Technology, 5600 MB, Eindhoven, The Netherlands*

<sup>4</sup>*Advanced Light Source, Lawrence Berkeley National Laboratory, 1 Cyclotron Road, Berkeley CA 94710, USA*

<sup>5</sup>*Nevada Extreme Conditions Laboratory, University of Nevada, Las Vegas, Las Vegas, Nevada 89154, USA*

<sup>6</sup>*Institute of Materials for Electronics and Energy Technology (i-MEET), Department of Materials Science and Engineering, Friedrich-Alexander-Universität Erlangen-Nürnberg, 91058 Erlangen, Germany*

<sup>7</sup>*Sorbonne Université CNRS, Collège de France, UMR 7574, Chimie de la Matière Condensée de Paris, Paris 75005, France*

<sup>8</sup>*Institut Photovoltaïque d'Île de France (IPVF), CNRS, Ecole Polytechnique, Palaiseau, 91120, France*

† equally contributing first authors

\*E-mail: [csutterfella@lbl.gov](mailto:csutterfella@lbl.gov)

## Abstract

Triple cation, mixed halide perovskite compositions have been reported to be more thermally stable, exhibit less phase impurities, show higher power conversion efficiency and better reproducibility than single cation perovskites. In this work, we explain the formation of  $\text{Cs}_{0.05}\text{FA}_{0.81}\text{MA}_{0.14}\text{Pb}(\text{I}_{0.85}\text{Br}_{0.15})_3$  via a multimodal in situ study combining structural information from grazing-incidence wide-angle synchrotron X-ray scattering (GIWAXS) and optical properties from photoluminescence (PL) spectroscopy with density functional theory calculations (DFT). The focus

here is on the effect of the solvent and antisolvent during crystallization. The predominantly used solvents N,N-dimethylformamide (DMF), dimethyl sulfoxide (DMSO), and the antisolvent chlorobenzene (CB) as well as the solvent-antisolvent-precursor interactions are investigated. Given the high elemental complexity and mutual interdependencies between solvent, antisolvent and perovskite precursors, we found significant differences in the crystallization pathways. DMF-pure precursors show the formation of the DMF-containing intermediate phase and the nucleation of compositionally distinct perovskite phases, while when DMSO is added only crystalline  $\alpha$ - and  $\delta$ - phases were found. In addition, the presence of DMSO helps the formation of  $\alpha$ -perovskite. Coordination energy and bond order (BO) calculations support our experimental findings. Dripping of CB induces nucleation at room temperature, slows down the  $\alpha$ -phase formation rate, and appears to reduce the nucleation radius. These findings provide novel insights into solvent, antisolvent, and perovskite precursor interactions and their formation pathways. The complexity of interactions between solvents and reagents highlights the importance of understanding these effects to further improve reproducibility and optimize processing conditions.

## **Introduction**

Hybrid halide perovskites are an unprecedented class of semiconductors with outstanding optoelectronic properties and thus, broad device application.<sup>1-3</sup> The crystal structure with a chemical formula  $ABX_3$  consists of an extended inorganic 3D network of  $BX_6$  octahedra surrounded by A-site cations. A and B are mono- and divalent- cations e.g.,  $CH_3NH_3^+$  (methylammonium, MA),  $CH(NH_2)_2^+$  (formamidinium, FA),  $Cs^+$  and  $Pb^{2+}$ , respectively, and X is a halide anion.

A myriad of synthetic approaches have been developed and continue to evolve.<sup>4</sup> The majority of halide perovskite syntheses follows a "one-step" chemical solution synthesis. Here, the organic and inorganic precursor

solutes are dissolved in a solvent, often followed by spin-coating deposition and subsequent annealing. The most commonly used solvents for halide perovskite solution synthesis are polar aprotic solvents including N,N-dimethylformamide (DMF), dimethyl sulfoxide (DMSO), gamma-butyrolactone (GBL), N-Methyl pyrrolidone (NMP) and mixtures thereof (see overview in the pie charts in Figure 1). The role of the solvent is not only to dissolve the reagents but also to participate in the perovskite crystallization process. Polar aprotic solvents can act as Lewis bases binding to  $\text{Pb}^{2+}$  acting in turn as the corresponding Lewis acid.<sup>5</sup> The perovskite precursor solutions are reported to be colloidal dispersions instead of true solutions where the solutes can complex with the solvent and form colloidal particles with up to the mesoscale sizes.<sup>6</sup> The colloid consists of a structurally tunable lead polyhalide framework which can affect morphology and film coverage.<sup>6,7</sup> Indeed, throughout literature, formation of stable bonds with ligands (e.g. with DMSO, thiourea, NMP) has been linked with nucleation and morphology control.<sup>8-11</sup> In addition, the properties of the solvents (Table 1) can influence the film drying characteristics and processing parameters such as the ideal wet film processing time window.<sup>12</sup> DMF has an almost ten times higher vapor pressure compared to DMSO leading to a higher solvent evaporation rate. Mixing of DMF with DMSO can reduce the evaporation rate and consequently widen the processing window.<sup>4,12</sup> The inverse of Mayer Bond Order (MBO) is a good measure of Pb solubilization. DMSO has a stronger interaction ability with  $\text{Pb}^{2+}$  species compared to DMF owing to its higher Gutmann donor number (29.8 vs 26.6 kcal/mol).<sup>13</sup> As will be discussed later, the solvent-precursor interactions quantified by coordination energy and bond order (BO) calculations play a significant role in understanding crystallization pathways and thin film fabrication design. See Table 1 for several of these properties.

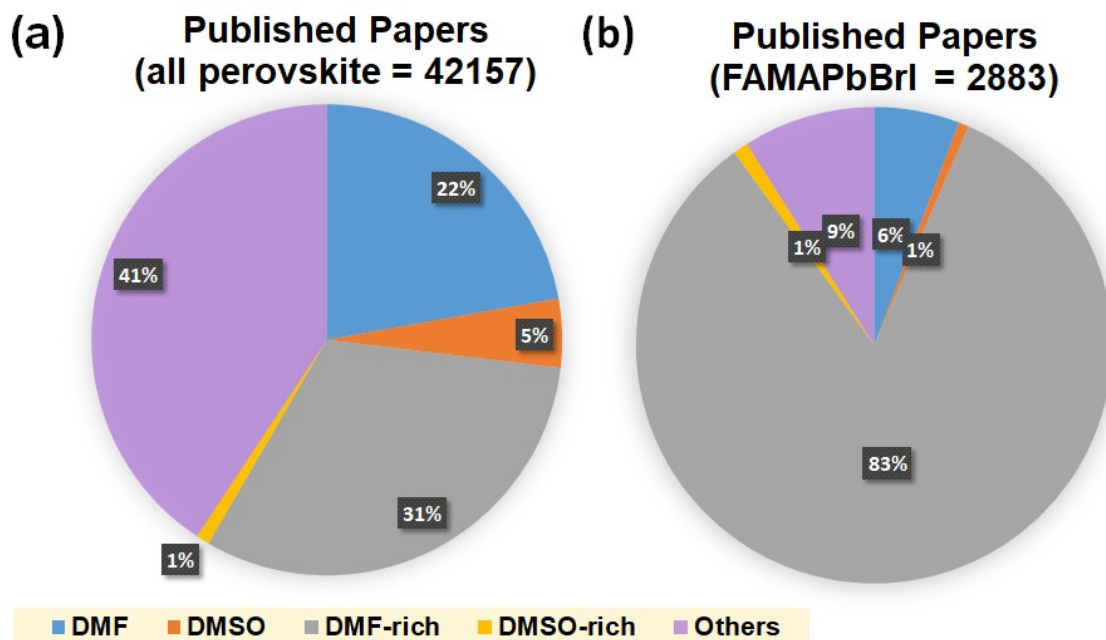


**Figure 1.** Pie chart of total published papers using different solvents and combinations thereof. (a) For all perovskite compositions, and (b) for (FA,MA)Pb(Br,I)<sub>3</sub> perovskite compositions. Others (purple) include  $\gamma$ -butyrolactone (GBL), Isopropyl Alcohol (IPA), and N-Methyl-2-pyrrolidone (NMP). This figure made use of the open-access Perovskite Database Project: <https://www.perovskitedatabase.com/>

**Table 1.** Solvent properties for DMF and DMSO used for mixed perovskite thin films.<sup>4,13,14</sup> Antisolvent properties for CB.<sup>15,16</sup>

Solvent	Density (g/mL)	Boiling Point (°C)	Viscosity (mPa s)	Vapor Pressure (mmHg, 20°C)	Enthalpy of Solvation $\Delta H_{\text{solv:Pb}^{2+}}$ (kcal mol <sup>-1</sup> )	Mayer Bond Order	Gutmann's donor number $D_N$ (kcal mol <sup>-1</sup> )	Hildebrand solubility parameter $\delta$ (Mpa <sup>1/2</sup> )
DMF	0.948	153	0.92	516	- 403	1.88	26.6	24.8
DMSO	1.10	189	2.0	55.6	- 412	1.50	29.8	26.7
CB	1.11	132	0.806	8.8	N.A.	N.A.	3.3	19.6

---

**N.A. = Not Available**

To date several in situ studies have been performed to investigate the formation pathways of halide perovskites during synthesis to elucidate structure formation and evolution of optical properties.<sup>17-22</sup> The goals of such studies are to better understand synthesis-structure-property relationships, improve reproducibility, and ultimately obtain high-quality perovskite films. In this work, we present a multimodal in situ study on the formation of  $\text{Cs}_{0.05}\text{FA}_{0.81}\text{MA}_{0.14}\text{Pb}(\text{I}_{0.85}\text{Br}_{0.15})_3$  by combining crystal structural information from grazing-incidence wide-angle synchrotron X-ray scattering (GIWAXS) and optical properties from photoluminescence (PL) spectroscopy with coordination energy and BO calculations. The focus of the present study is on the influence of the solvents DMF, DMSO and mixtures thereof, on the crystallization pathway. In addition, we are looking at the effect and event of antisolvent (chlorobenzene, CB) dripping. It is shown that DMF not only gives rise to the intermediate DMF-containing phase but also the nucleation of compositionally distinct species. Our study provides an explanation of why mixed DMF:DMSO precursor solutions in combination with CB lead to better film quality. In the presence of DMSO, there is no crystalline solvate-intermediate phase and only  $\alpha$ - and  $\delta$ -phases were observed when applying antisolvent for the triple cation and mixed halide perovskite composition under study. There is a signature of the formation of an amorphous film before the crystallization onset when DMSO is added and without applying antisolvent. Moreover, DMSO inhibits compositionally distinct nucleating species which appear to have an influence on film quality and stability. Dripping of CB induces nucleation at room temperature, reduces the nucleation radius, and slows down the overall  $\alpha$ -phase formation rate. The complexity of interactions between solvent, antisolvent, and precursor

constituents highlights the need for in situ characterizations to improve synthesis design and reproducibility.

## Results and Discussion

The focus of this study is on the film formation using the most frequently used solvent system DMF-rich (DMF/DMSO with 4:1, v/v) in comparison with pure DMF solvent as reference synthesis condition, with and without CB antisolvent dripping. The multimodal results from in situ diffraction and PL are summarized in Figure 2 (additional data including 2D diffraction images, integrated scattering intensities near  $q \approx 1.0 \text{ \AA}^{-1}$ , and scanning electron microscopy images are shown in Figures S1–S5 in the supplementary information, SI). For DMF pure samples prepared without antisolvent (Figure 2a-d), the crystallization occurs after 12 seconds from the start of the spin coating as revealed by the evolution of clear diffraction peaks. The peaks near  $q \approx 0.46$ ,  $0.56$ , and  $0.67 \text{ \AA}^{-1}$  are associated with the intermediate DMF-containing phase  $(\text{MA})_2(\text{DMF})_2\text{Pb}_3\text{I}_8$ . Please note that the exact composition may deviate due to the co-presence of other cations and anions. A more general expression would be  $\text{A}_2(\text{DMF})_2\text{Pb}_3\text{X}_8$  (where A can be a mixture of Cs, FA, and MA and X can be I and Br) therefore it will be referred to as DMF-containing intermediate, whereas the peaks near  $q \approx 0.83$  and  $1.0 \text{ \AA}^{-1}$  are associated with  $\delta$ - (hexagonal) and  $\alpha$ - (cubic)<sup>23</sup> perovskite phases, respectively. A similar behavior is observed when applying an antisolvent showing the evolution of the DMF-containing intermediate,  $\delta$ - and  $\alpha$ -phases. According to the literature, the previously reported DMF-containing intermediate phase is induced from DMF-complexes in solution.<sup>24,25</sup> In general, the larger FA cation as compared to the MA cation gives rise to a relatively larger Goldschmidt tolerance factor.<sup>26</sup> This leads to room-temperature instabilities of the desired  $\alpha$ -phase and consequently, the formation of  $\delta$ -phase, which is a non-perovskite phase with hexagonal structure.<sup>17,27</sup> The initial PL emission signal centered  $\approx 1.7$ - $1.75 \text{ eV}$  (Figure

S6, SI) is possibly associated with the nucleation of the perovskite phase, a luminescent intermediate phase containing 2D-layered nanosheets, or other low dimensional perovskite clusters as the  $\delta$ -phase emission is at higher energy.<sup>28</sup> Reduction in dimensionality leads to a blue shift of the PL signal in comparison to the bulk bandgap due to quantum confinement as shown by several prior reports.<sup>29-31</sup> Bright PL emission is observed during the spin coating stage consistent with the formation of perovskite phase as revealed by GIWAXS while the emission is mostly quenched during thermal annealing (Figure 2b,d bottom). The absence of other distinct PL peaks may be related to the laser excitation energy ( $\approx 2.3$  eV) which limits excitation to phases with bandgaps  $\leq 2.3$  eV, low radiative recombination rate compared to total recombination rate, and carrier funneling to lower bandgap regions<sup>32</sup>. PL is sensitive to materials with high radiative recombination rate including small crystallites (nuclei) effectively complementing GIWAXS measurements because they may not lead to detectable diffraction signal due to short range order or small volume fraction in the total film as found in previous works<sup>20,33</sup>. The diffraction and PL provide complementary information during the initial stages of crystallization. PL indicates very small crystallites (nuclei or clusters) while larger crystallites give rise to diffraction peaks. Those nuclei or clusters could lead to the quantum confinement and PL at higher energies as it was shown experimentally by Parrott et al.<sup>29</sup>.

With the addition of DMSO as solvent or co-solvent with DMF (DMF-rich), the DMF-containing intermediate phase formation is not observed (Figure 2e-h). In order to evaluate to which degree the solvent-precursor interaction influences the interplay between perovskite and  $\delta$ -phase formation as well as appearance of intermediate phases, we also investigated the pure DMSO and DMSO-rich (DMSO/DMF with 7:3, v/v) solvent systems and fabricated  $\text{Cs}_{0.05}\text{FA}_{0.81}\text{MA}_{0.14}\text{Pb}(\text{I}_{0.85}\text{Br}_{0.15})_3$  without and with CB (Figure S7, SI). Despite the stronger coordination ability of DMSO, no DMSO adducts (such as  $(\text{MA})_2\text{Pb}_3\text{I}_8 \cdot 2\text{DMSO}$ ,  $\text{PbI}_2 \cdot 2\text{DMSO}$ ) were found. The interaction between DMSO

and FAI was reported to be weak or negligible<sup>5</sup> and no crystalline phases containing solely FA, I, and DMSO is expected which is in line with experiments conducted by Petrov et al.<sup>34</sup> During spin coating and before reaching the final annealing temperature there is a signature of an amorphous phase spanning  $q \approx 0.4-0.6 \text{ \AA}^{-1}$  possibly associated with scattering from the bulk solvent. Thermal annealing is needed to initiate crystallization for the film prepared without antisolvent. Given the one order of magnitude lower vapor pressure of DMSO (Table 1), the solvent evaporation rate is slowed down and no crystalline phases form during spin coating. A recent density functional theory and ab-initio molecular dynamics study showed that mixing of DMF with small amounts of DMSO results in more balanced reaction energies favoring high-I-coordinated iodoplumbates, and importantly, corner-sharing  $\text{PbI}_x$  complexes which may serve as nucleation sites to form perovskites.<sup>35</sup> Further, it was speculated that the better energetic balance may correlate with a more equilibrated crystallization process in the presence of DMSO. Coordination energy and bond order calculations discussed below confirm these findings for mixed cation and mixed halide perovskites. With antisolvent dripping around 25 s, crystallization starts during spin coating and the  $\delta$ -phase ( $q \approx 0.83 \text{ \AA}^{-1}$ ) appeared first, and temporally close to the perovskite phase ( $q \approx 1.0 \text{ \AA}^{-1}$ ). While the  $\delta$ -phase appears first in the synthesis with antisolvent during spin coating and at room temperature, it appears together with the perovskite phase in the synthesis without antisolvent during thermal annealing (Figure S3, SI). This observation hints that both phases form competitively during early crystallization stages while it is known that the  $\delta$ -phase is energetically more favorable at room temperature. Thus, the  $\delta$ -phase formation is less prevalent in the synthesis without CB where phase formation requires thermal annealing and the cubic  $\alpha$ -phase has a higher stability.<sup>17,36</sup> The  $\delta$ -phase is relatively short-lived in the DMF-rich case and dissociates during spin coating but persists longer in the case with pure DMF and starts to disappear only during annealing around  $\sim 100 \text{ s}$  when reaching  $\sim 55 \text{ }^\circ\text{C}$



(temperature profiles as tracked by a pyrometer during synthesis are visible in Figure S8, SI). In the DMF-rich solvent system, PL during spin coating i.e. at room temperature is only observed when an antisolvent is used (Figure 2g bottom). Without antisolvent, PL emission is only observed during the annealing step. This is in agreement with the GIWAXS results which show perovskite formation upon antisolvent dripping or during annealing in the absence of an antisolvent.

Taking a closer look at the integrated diffraction rings around  $q \approx 1 \text{ \AA}^{-1}$  (Figure 3), two distinct peaks with  $q \approx 1.00$  and  $q \approx 1.04 \text{ \AA}^{-1}$  can be identified in the early crystallization stages for the DMF-pure sample. This peak splitting indicates diffraction from perovskite lattices with different unit cells. The peak at  $q \approx 1.04 \text{ \AA}^{-1}$  corresponds to a smaller unit cell compared to the peak at  $q \approx 1 \text{ \AA}^{-1}$ , likely due to incorporation of a larger content of smaller elements such as Br or Cs on the X and A sites, respectively. With antisolvent, the  $q \approx 1.04 \text{ \AA}^{-1}$  dominates over  $q \approx 1.00 \text{ \AA}^{-1}$  initially (Figure 3b). During annealing, the  $q \approx 1.04 \text{ \AA}^{-1}$  diminishes while the intensity of the  $q \approx 1.00 \text{ \AA}^{-1}$  increases. This behavior hints at a correlation between the two peaks. To further confirm that this additional peak (around  $q \approx 1.04 \text{ \AA}^{-1}$ ) is not associated with other intermediate phases, we show in **Figure S9a, SI**, simulated XRD patterns of expected competing phases calculated from CIF files for  $\alpha$ -FAPbI<sub>3</sub>-cubic,  $\alpha$ -FAPbI<sub>3</sub>-tetragonal,  $\delta$ -FAPbI<sub>3</sub>-hexagonal, MA<sub>2</sub>(DMF)<sub>2</sub>Pb<sub>3</sub>I<sub>8</sub>, and MA<sub>2</sub>(DMSO)<sub>2</sub>Pb<sub>3</sub>I<sub>8</sub> phases. None of the competing phases has peak overlap with the additional peak (around  $q \approx 1.04 \text{ \AA}^{-1}$ ) except for MA<sub>2</sub>(DMSO)<sub>2</sub>Pb<sub>3</sub>I<sub>8</sub>. This phase cannot appear in samples prepared from pure DMF. Thus, we attribute this additional peak to the perovskite  $\alpha$ -phase (either cubic or tetragonal). However, during spin coating, we can't distinguish if the  $\alpha$ -phase is cubic or tetragonal since the peaks that distinguish between the cubic and tetragonal phases overlap with peaks associated with the intermediate phases (**Figure S9a, SI**). For instance, the additional tetragonal peak (around  $q \approx 1.55 \text{ \AA}^{-1}$ ) overlaps with peaks of the

intermediate phases  $\text{MA}_2(\text{DMF})_2\text{Pb}_3\text{I}_8$  and  $\delta\text{-FAPbI}_3$ -hexagonal (**Figure S9a, SI**). Other higher order peaks of tetragonal phase also overlap with peaks associated with the intermediate phases. The annealed films have peak signatures of the cubic  $\alpha$ -phase (**Figure S9b+c, SI**). It was described previously for triple cation halide perovskites with similar composition as under investigation here ( $\text{Cs}_{0.1}\text{FA}_{0.7}\text{MA}_{0.2}\text{Pb}(\text{I}_{0.8}\text{Br}_{0.2})_3$ ) but in mixed DMF/DMSO that the nuclei are Br-rich because Br-rich species have lower solubility due to a weaker bond with DMSO compared to iodine.<sup>37</sup> While the study by Huang et al. reported Br-rich nucleation followed by homogenization through iodine (I) incorporation i.e. a shift in the diffraction position, our study shows two chemically distinct nucleation species for the DMF-pure precursors. Here, we hypothesize that formation of the DMF-containing intermediate phase is dominant during initial crystallization consuming a significant amount of MA and I ions. To support this hypothesis, we have calculated the volume ratio of DMF-containing intermediate phase to the perovskite  $\alpha$ -phase using methodology detailed previously.<sup>17</sup> The volume ratio of DMF-containing intermediate phase to perovskite phase is 11.8 : 1 and 10.3 : 1 for pure DMF samples prepared without and with antisolvent, respectively. These values confirm the dominance of the DMF-containing intermediate phase as compared to the perovskite  $\alpha$ -phase. Consequently, the  $\alpha$ -phase is expected to incorporate more of the remnant smaller ions (Cs and Br) leading to the formation of a peak near  $q \approx 1.04 \text{ \AA}^{-1}$ . The broader peak near  $q \approx 1.0 \text{ \AA}^{-1}$  occurring simultaneously can be associated with the I-rich  $\alpha$ -phase. One explanation for this observation and in agreement with DFT calculations below is that elemental segregation is initiated in solution where DMF strongly binds to MA and I to form colloids of DMF-complexes associated with the DMF-containing intermediate phase. Once DMSO is added to the triple cation mixed halide precursor, DMF-complexes are suppressed due to a comparatively weak coordination energy of DMSO-MAI (-0.65 eV) as compared to DMSO-PbI<sub>2</sub> (-1.02 eV), see Figure 4. More discussion on the calculations can be found below. Figures 3c,d and S10 illustrate the absence

of an additional peak around  $q \approx 1.04 \text{ \AA}^{-1}$  in any systems containing DMSO. Fig. S11 illustrates the higher order  $\alpha$ -phase peaks of the DMF system with  $q \approx 2.0 \text{ \AA}^{-1}$ . It is speculated that mixed DMF-DMSO solutions are more homogenous in the absence of large colloids which leads to the homogeneous nucleation of only one perovskite composition. The heterogeneity in solution and initial compositionally distinct perovskite crystallization in pure DMF solvent possibly have negative effects on the film quality and stability of perovskite films which might make them more prone to phase segregation.

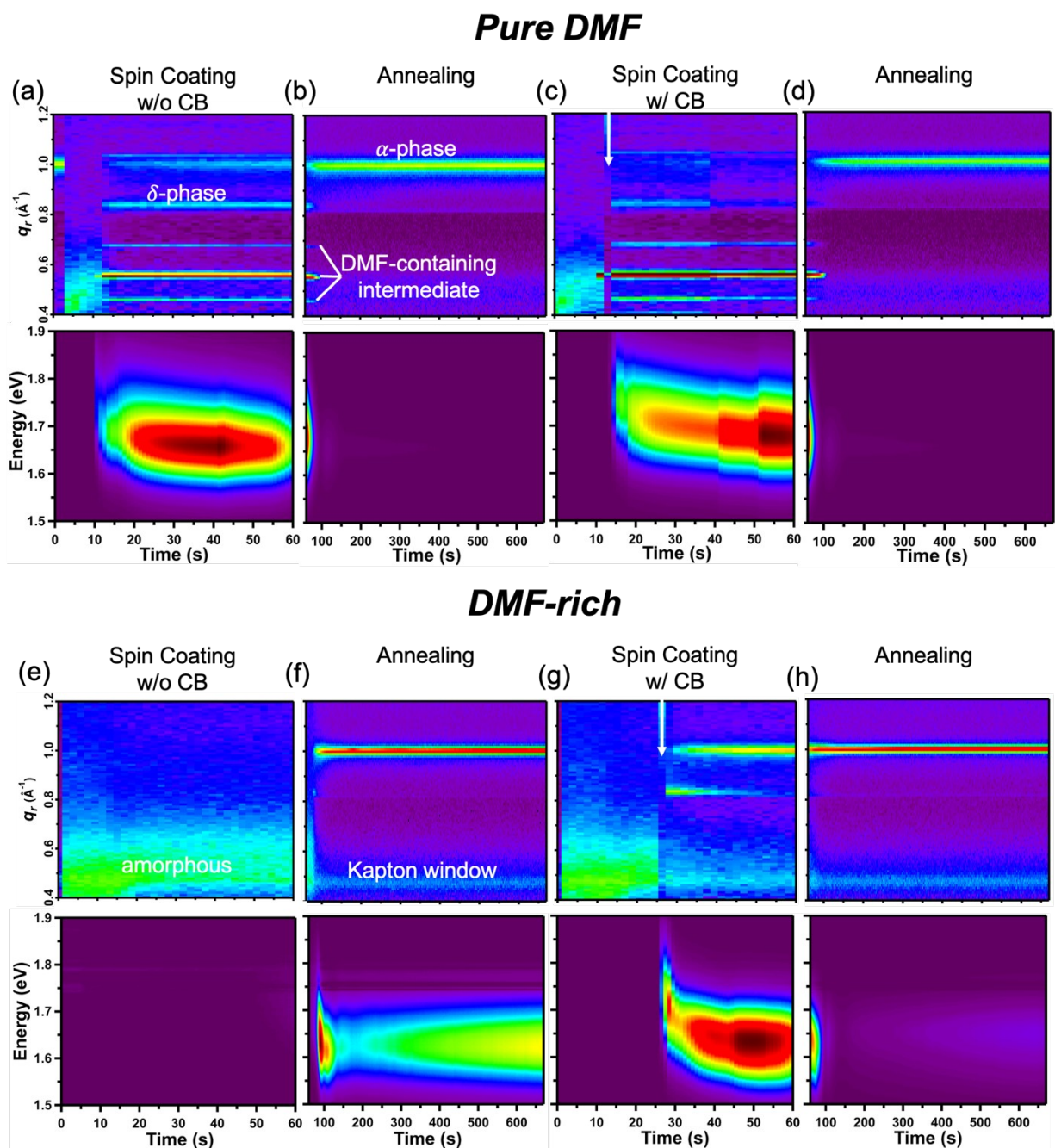


**Figure 2** In situ GIWAXS and PL contour plots recorded during the formation of  $\text{Cs}_{0.05}\text{FA}_{0.81}\text{MA}_{0.14}\text{Pb}(\text{I}_{0.85}\text{Br}_{0.15})_3$  from pure DMF (a-d) and DMF-rich (DMF/DMSO = 4:1, v/v) precursors (e-h). The left-hand side for each solvent system shows the spin coating step and the right-hand side the annealing step. Samples in c, d, g and h were prepared using antisolvent dripping (chlorobenzene drip indicated by the white arrow), whereas the remaining samples were prepared without antisolvent. The appearance of a vertical 'line' over the full  $q$  space for samples with antisolvent is attributed to the

dispersion of the antisolvent which blocks the view to the detector. In addition, the broad peak at  $\approx 0.47 \text{ \AA}^{-1}$  is from the Kapton window of the spin coater setup. Discrete intensity fluctuations in PL can occur when the sample slightly moves, e.g. when the remotely controlled heating is triggered.

All PL spectra show an initial red shift (Figure S6, SI) which has been reported earlier by several groups and for various perovskite compositions.<sup>22,33,38</sup> In general, the red shift can be associated with either change of size or composition. For example, forming a Br- or Cs-rich phase or small quantum-confined crystallites will lead to wider bandgaps and higher energy emission. In situ GIWAXS did not indicate Br-rich nuclei for DMF-rich samples because the peak around  $q \approx 1.00 \text{ \AA}^{-1}$  is constant in position (Figure 3c,d), while it shows a very small shift in the DMF-pure samples (Figure 3a,b) therefore, a convoluted effect of quantum confinement and compositional variation cannot be excluded to explain the blue shifted PL.

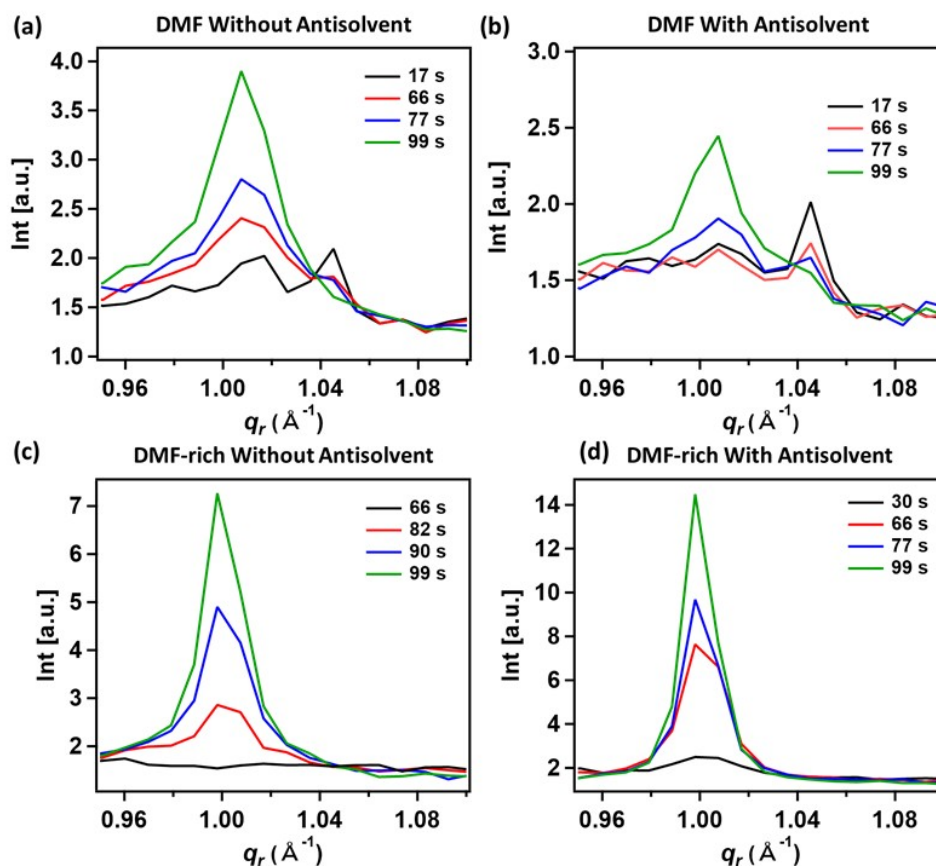


**Figure 3.** Radially integrated diffraction intensity for DMF and DMF-rich solvent systems without and with antisolvent. The peak around  $q \approx 1 \text{ \AA}^{-1}$  corresponds to the  $\alpha$ -phase of triple cation perovskite. The times indicated are from the start of the spin coating.

To gain further insights regarding impact of the type of solvents and solvent-precursor interaction on the crystallization pathways, we calculate the coordination energy and BO of these species, including solvents (DMF and DMSO), precursors (MAI, FAI, CsI,  $\text{PbI}_2$ ,  $\text{PbBr}_2$ ) and antisolvents (CB). In general, the lower the coordination energy between species the more energetically favorable is their formation and the higher the BO, the stronger the covalent bond. The main findings are summarized in Figure 4, and details of the energies and bond order can be found in Table S1, SI. All coordination's are found to be energetically favorable, in the range of about -0.1 to about -1 eV. Focusing on the coordination between DMF and precursors, due to the less energetically favorable coordination with FAI- (-

0.69 eV, BO: 0.15) than MAI (-0.84 eV, BO: 0.17), DMF preferentially coordinates with MAI at first, followed by FAI. In addition, the magnitude of the coordination energies of DMF with  $\text{PbI}_2$  (-0.95 eV) and with MAI (-0.84 eV) are similar. We speculate that the very similar interaction energies and the Pb-rich condition (relative comparison of  $\text{PbI}_2:\text{MAI} > 3:2$ ) make the formation of the DMF-containing intermediate phase possible.<sup>24</sup> After its formation a significant portion of the  $\text{PbI}_2$  precursor has been consumed and the remaining solution is in a FAI-rich condition, possibly preventing the formation of the  $\text{FA}_2\text{Pb}_3\text{I}_8 \cdot 4\text{DMF}$  and  $\text{FA}_2\text{Pb}_2\text{I}_6 \cdot 4\text{DMF}$  intermediate phases reported by Petrov et al.<sup>34</sup> This is corroborated by the fact that the only FA-containing intermediate phase, reported by Petrov, was observed for a pure  $\text{FAPbI}_3$  precursor in DMF, but not in DMSO. Upon adding 25% of Br,  $\text{FAPb}(\text{I}_{0.75}\text{Br}_{0.25})_3$ , no FA intermediate phase was observed irrespective of the solvent and in agreement with our experimental work.<sup>24</sup>

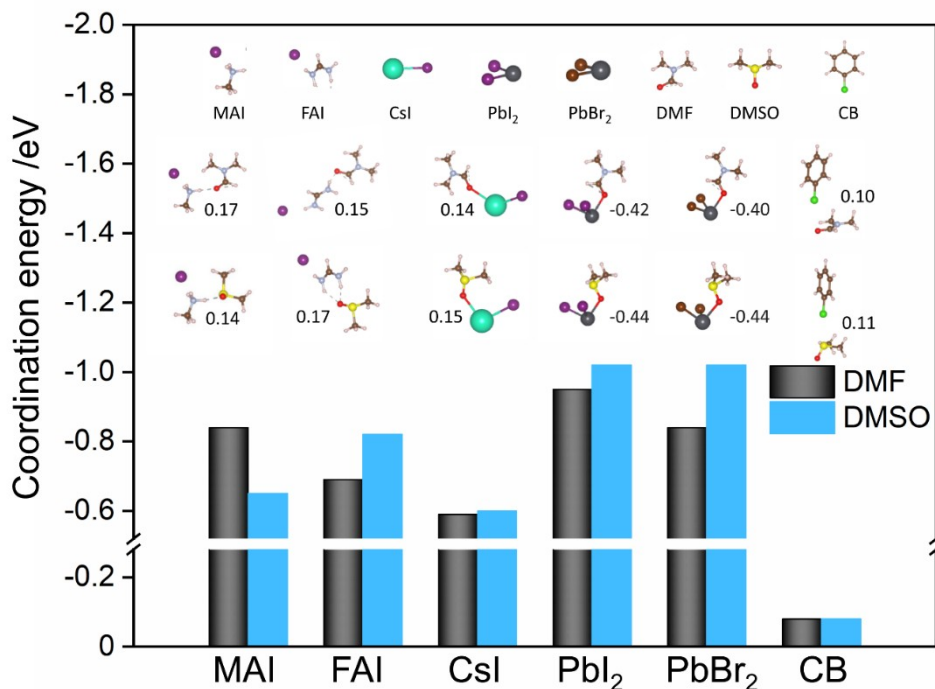


**Figure 4.** The coordination energy of solvents (DMF and DMSO) with precursors (MAI, FAI, CsI,  $\text{PbI}_2$  and  $\text{PbBr}_2$ ) and also with antisolvent (CB). The values next to the structure represent the bond order of the bond between precursors and solvents.

Adding DMSO to DMF in comparison to pure DMF, the coordination energy of DMSO-MAI (-0.65 eV, BO of DMSO-MAI: 0.14) is significantly weaker than DMSO-PbI<sub>2</sub> (-1.02 eV, BO of DMSO-PbI<sub>2</sub>: 0.44). The stronger coordination of DMF-MAI than DMSO-MAI can be attributed to the stronger hydrogen bond in DMF-MAI. Consequently, if replacing DMF by DMSO or mixing DMSO into the DMF solvent system, the coordination of DMSO with PbI<sub>2</sub> dominates and prevents the formation of the intermediate phase, explaining the absence of the DMF-containing intermediate phase in our experiments.

DFT provides a possible explanation for the early crystallization stages with two diffraction peaks in the pure DMF case (illustrated in Figure 3) by noting the weaker coordination of DMF-PbBr<sub>2</sub> (-0.84 eV, BO: 0.40) compared to DMF-PbI<sub>2</sub> (-0.95 eV, BO: 0.42), Figure 4. This indicates that the nucleation of Br-rich domains may occur earlier than I-rich domains and is consistent with the peak changes shown in Figure 3a and 3b. Interestingly, incorporating DMSO into DMF suppressed the Br-rich nucleation centers, due to the very similar coordination strength between DMSO-PbBr<sub>2</sub> and DMSO-PbI<sub>2</sub> (the same coordination energy of -1.02 eV and same BO of 0.42 shown in Figure 4). We note that although the amount of DMF is higher than DMSO in the mixed solvent, PbX<sub>2</sub> is predicted to coordinate with DMSO first due to the larger coordination strength compared with DMF. Therefore, it is likely that there are no preferred Br-rich nucleation centers, consistent with the observation shown in Figure 3c and 3d. We also studied the coordination between CsI-solvents as the Cs cation could also be involved in the early nucleation stages. Figure 4 indicates that although two diffraction peaks ( $q \approx 1.00$  and  $q \approx 1.04 \text{ \AA}^{-1}$ ) in the DMF solution could also be attributed to the weaker coordination of CsI-DMF (-0.59 eV, BO:0.14) than that of MAI-DMF(-0.84 eV, BO: 0.17) and FAI-DMF(-0.69 eV, BO: 0.15), the much weaker coordination of CsI-DMSO (-0.60 eV, BO:0.15) than FAI-DMSO (-0.82 eV, BO: 0.17) could not



explain why there is no diffraction peak change in the DMF-DMSO solution. We speculate that the effect of the Cs cation is mostly on its interactions with  $\text{PbX}_2$  species, the Cs cation bonds  $\text{PbX}_2$  species stronger than MA/FA cation because of strong electrostatic/ionic interactions and also the less competition in coordinating with the solvents. Because of this, the Cs cation helps to form 3D triple cation perovskites. The impact by solvent type is minimal and secondary. Therefore, the dynamics shown in Figure 3 are more likely to result from the Br-rich nucleation than the Cs-nucleation.

Focusing on the antisolvent, we find almost identical coordination values of CB with both solvents (Figure 4) and more structure configurations are illustrated in Figure S12, SI. This demonstrates that CB is unlikely to play a significant role in the formation of intermediate phases. Instead, the coordination between CB and solvents indicates its ability in the extraction of solvents from precursors, following a supersaturation period and acceleration of nuclei formation, which is consistent with our experimental observation.

This study provides experimental in situ data and insights from DFT to explain the benefit of mixed DMF:DMSO precursor solutions in combination with CB showing that small additions of DMSO help the  $\alpha$ -phase formation. It also leads to the nucleation of compositionally uniform perovskite crystallites, possibly because of very similar coordination strength between DMSO- $\text{PbBr}_2$  and DMSO- $\text{PbI}_2$ . For DMF pure precursors, large DMF colloids lead to the dominant DMF-containing intermediate phase. Formation of this phase possibly leads to nucleating perovskite species with different compositions detrimental for the final film quality. The intermediate DMF-containing phase is absent in the presence of DMSO.



## Experimental & Methods

To visualize the frequency of typical solvents used by the perovskite community, we made use of the open-access Perovskite Database Project (<https://www.perovskitedatabase.com/>) recently introduced and published by Jacobsson et al.<sup>39</sup>

### Materials

Lead iodide (PbI<sub>2</sub>, 99.99%), and Caesium iodide (CsI, 99.99%) were purchased from TCI. Formamidinium iodide (FAI) and methylammonium bromide (MABr) were purchased from Greatcell Solar. Lead bromide (PbBr<sub>2</sub>), dimethylformamide (DMF), dimethyl sulfoxide (DMSO), and chlorobenzene (CB) were purchased from Sigma-Aldrich (USA). All chemicals listed were used as received without further purification.

### Solution Preparation and Film Fabrication

Mixed cation and halide perovskite precursor were prepared by dissolving PbI<sub>2</sub> (460 mg), FAI (167 mg), MABr (18.8 mg), PbBr<sub>2</sub> (61.5 mg), and CsI (15.6 mg) in anhydrous polar aprotic solvents (DMF and DMSO) with total volume of 1 ml resulting in Cs<sub>0.05</sub>FA<sub>0.81</sub>MA<sub>0.14</sub>Pb(I<sub>0.85</sub>Br<sub>0.15</sub>)<sub>3</sub>. The solvent ratios for DMF- and DMSO-rich are DMF:DMSO = 800:200  $\mu$ L and DMF:DMSO = 290:710  $\mu$ L. Precursors were heated at 50 °C and stirred at 500 rpm for 4-5 h. Glass substrates were used to fabricate perovskite thin films. Glass substrates were cleaned by following the cleaning sequence of detergent, deionized water, acetone, and IPA washing. Before perovskite precursor deposition, the glass substrates were cleaned with a plasma cleaner. Perovskite thin films were fabricated through spin-coating using 1000 rpm for 10s and 4000 rpm for 30s followed by annealing at 100 °C for 10 min. Chlorobenzene was used as an antisolvent (100  $\mu$ L) and dripped at 17s for pure DMF and pure DMSO and at 25 s for DMF- and DMSO-rich precursors.

## **Multimodal Characterization - *In situ* synchrotron Grazing-incidence wide-angle X-ray scattering (GIWAXS) and *In situ* Photoluminescence (PL)**

Grazing-incidence wide-angle X-ray scattering (GIWAXS) was performed during spin coating and thermal annealing in a custom made spin coater attached to beamline 12.3.2 at the Advanced Light Source (ALS), Lawrence Berkeley National Laboratory. The custom-made setup allows to fabricate thin films via solution synthesis and antisolvent dripping in the hutch, using one sample stage for spin coating and annealing while collecting diffraction and PL data. The incoming X-ray beam was at a shallow angle of  $1^\circ$  with a beam energy of 10 keV. A DECTRIS Pilatus 1M X-ray detector at an angle of  $40^\circ$  to the sample plane and a sample to detector distance of  $\sim 164$  mm was used. Measurements were carried with an approximate flux of  $\sim 10^9$  photons  $s^{-1}$  on an area of  $0.1$  mm<sup>2</sup> ( $10$  mm  $\times$   $0.01$  mm) for 10 min. The spin coater setup is designed in such a way that the experiment can be performed remotely avoiding any delays or transfer times between film deposition and annealing. Measurements are conducted under an overpressure of N<sub>2</sub>. Samples were heated using a ramping speed of  $2^\circ\text{C s}^{-1}$  which takes  $\sim 120$  s to stabilize the temperature at  $100^\circ\text{C}$ . The diffraction data was collected with a frame rate of  $1.875$  s<sup>-1</sup>. The 2D diffraction images were analyzed using Image J software. All the *in situ* GIWAXS and *in situ* PL data were further analyzed by using Igor Pro 8.04 software. PL spectra were collected simultaneously using a 532 nm laser diode with a maximum power density of  $\sim 5$  mW cm<sup>-2</sup>, fiber coupled to a QE pro spectrometer from Ocean optics using a 550 nm long-pass filter. PL data were collected every second. The extent of beam damage depends on photon flux, energy of the X-rays and exposure time as well as the measurement atmosphere.<sup>40</sup> Another factor to consider is the actual X-ray absorption in the film which is element and energy specific. While the beam energy used here was 10 keV, Pb has an absorption edge near 13.03 keV meaning that X-ray absorption is much lower than at X-ray energies  $> 13$  keV. Stronger absorption can lead to a

higher absorbed X-ray dose and consequently higher beam damage rate. Beam damage or radiation-induced structural damage is often apparent by a decrease in scattering intensity of the Bragg peaks. It can also lead to a peak position shift and appearance of  $\text{PbI}_2$ . Following the recommendations by Hoye et al.<sup>40a</sup> a comparatively low photon flux, inert atmosphere ( $\text{N}_2$ ), and an X-ray energy below the absorption edge of Pb was chosen for the in situ measurements. It is noted that the signature of radiation-induced structural damage is more straightforward to interpret in 'static' measurements of fully fabricated films. The challenge with characterizing films *during* fabrication is that phase evolution or growth manifests in an increase of the scattering intensity. Thus, beam-induced effects cannot fully be excluded. Investigation of beam damage on a fully fabricated film is shown in Figure S13.

### **Characterization of Perovskite Films**

Morphological characterization was performed using scanning electron microscopy (SEM). The SEM images were taken using a quanta FEG 250 at an electron beam voltage of 10kV. The samples were prepared in a  $\text{N}_2$ -filled glove box.

### **Density Functional Theory Calculations (DFT)**

The DFT calculations were performed in the Vienna Ab Initio Simulation Package (VASP)<sup>41-43</sup>. The calculations were performed with the generalized gradient approximation as proposed by Perdew, Burke, and Ernzerhof (PBE)<sup>44</sup>, with energy and force convergence parameters of  $1 \times 10^{-2}$  eV/Å, and a  $1 \times 10^{-5}$  eV, respectively. The long-range dispersive interactions between solvent molecules and precursors/CB were corrected by the DFT-D3 scheme<sup>45</sup>. The coordination energies were calculated as following:

$$E_{\text{Coordination}} = E_{\text{solvent-x}} - E_{\text{solvent}} - E_{\text{x}}$$

where solvent represents DMF/DMSO, x represents MAI,  $\text{PbI}_2$ , CsI, CsBr and chlorobenzene. All the calculation optimized models, adapted from the intermediate phases  $(\text{MA})_2(\text{DMF})_2\text{Pb}_3\text{I}_8$  and  $(\text{FA})_2(\text{DMF})_4\text{Pb}_3\text{I}_8$  as presented in

Figure S14, are shown in Figure S15. More detailed information can be found in the description of DFT structural models in the supporting information.

### **Chemical Bonding Analysis**

The chemical bonding character and strength between precursor and solvents were analyzed by calculating the bond order (the larger the bond order value, the stronger the covalent/hydrogen) by using the Density Derived Electrostatic and Chemical (DDEC6) method<sup>46,47</sup>. This approach has shown to be effective in the investigation of the qualitative trends in chemical bonding of several halide perovskites.<sup>48-50</sup>

### **Supporting Information.**

2D diffraction images at relevant times during thin film evolution, integrated diffraction intensity over time, scanning electron microscopy images, additional in situ photoluminescence data, simulated X-ray diffraction patterns for  $\alpha$ -FAPbI<sub>3</sub>-cubic,  $\alpha$ -FAPbI<sub>3</sub>-tetragonal,  $\delta$ -FAPbI<sub>3</sub>-hexagonal, MA<sub>2</sub>(DMF)<sub>2</sub>Pb<sub>3</sub>I<sub>8</sub>, and MA<sub>2</sub>(DMSO)<sub>2</sub>Pb<sub>3</sub>I<sub>8</sub> phases, description of DFT structural models, assessment of beam damage, optimized structures for DFT calculations.

### **Author contributions**

M.S., M.A., and C.M.S.-F. conceived the idea. M.S. and C.M.S.-F. designed the experiments. J.L.S. designed, engineered, and build the in situ spin coater attached to the diffraction beamline, as well as provided technical support. M.S., T.K. and M.A. performed the in situ WAXS and PL measurements supervised by C.M.S.-F. M.A. performed in depth in situ WAXS analysis. Q.L. performed DFT calculations and chemical bonding analysis supervised by S.T. S.A. assisted with visualizing the results. C.M.S.-F. wrote the original manuscript draft. D.-K.L., C.P.S. helped with the revision of the manuscript. D.R.C. conducted the beam damage measurements. All authors contributed feedback and commented on the manuscript.

### **Acknowledgments**

Work at the Molecular Foundry was supported by the Office of Science, Office of Basic Energy Sciences, of the U.S. Department of Energy under Contract

No. DE-AC02-05CH11231 and is gratefully acknowledged by M.S. and C.M.S.-F. This work used beamline 12.3.2 supported by Dr. Tamura at the Advanced Light Source (ALS), which is a DOE User Facility under Contract No. DE-AC02-05CH11231. M.A. acknowledges support by the US Department of Energy, Office of Science, Office of Basic Energy Sciences, Materials Sciences and Engineering Division under Contract No. DE-AC02-05-CH11231 (D2S2 program KCD2S2). T.K. acknowledges the German Research Foundation (DFG) for funding (fellowship number KO6414). C.J.B., S.A., and C.M.S.-F. acknowledge funding from the Bavaria California Technology Center (BaCaTeC) project No. 13 [2021-2]. S.T. acknowledges funding by NWO START-UP (Project No. 740.018.024) and VIDI (Project No. VI.Vidi.213.091) from the Netherlands. Q.L. acknowledges and the China Scholarship Council (CSC) (No. 201808440385). D.-K.L. and C.P.S. acknowledge Office of Science, Office of Basic Energy Sciences, of the U.S. Department of Energy under contract number DE-SC-0023355. D.R.C. and C.M.S.-F. acknowledge support from the France Berkeley Fund (FBF).

## References

- (1) Al-Ashouri, A.; Köhnen, E.; Li, B.; Magomedov, A.; Hempel, H.; Caprioglio, P.; Márquez, J. A.; Morales Vilches, A. B.; Kasparavicius, E.; Smith, J. A. Monolithic Perovskite/Silicon Tandem Solar Cell With > 29% Efficiency by Enhanced Hole Extraction. *Science* **2020**, *370* (6522), 1300–1309.
- (2) Jeong, J.; Kim, M.; Seo, J.; Lu, H.; Ahlawat, P.; Mishra, A.; Yang, Y.; Hope, M. A.; Eickemeyer, F. T.; Kim, M. Pseudo-Halide Anion Engineering for  $\alpha$ -FAPbI<sub>3</sub> Perovskite Solar Cells. *Nature* **2021**, *592* (7854), 381–385.
- (3) Liu, F.; Wu, R.; Wei, J.; Nie, W.; Mohite, A. D.; Brovelli, S.; Manna, L.; Li, H. Recent Progress in Halide Perovskite Radiation Detectors for Gamma-Ray Spectroscopy. *ACS Energy Lett.* **2022**, *7* (3), 1066–1085.
- (4) Dunlap-Shohl, W. A.; Zhou, Y.; Padture, N. P.; Mitzi, D. B. Synthetic Approaches for Halide Perovskite Thin Films. *Chem. Rev.* **2019**, *119* (5), 3193–3295.
- (5) Lee, J.-W.; Kim, H.-S.; Park, N.-G. Lewis Acid–Base Adduct Approach for High Efficiency Perovskite Solar Cells. *Acc. Chem. Res.* **2016**, *49* (2), 311–319.
- (6) Yan, K.; Long, M.; Zhang, T.; Wei, Z.; Chen, H.; Yang, S.; Xu, J. Hybrid Halide Perovskite Solar Cell Precursors: Colloidal Chemistry and Coordination Engineering behind Device Processing for High Efficiency. *J. Am. Chem. Soc.* **2015**, *137* (13), 4460–4468.
- (7) Shargaieva, O.; Kuske, L.; Rappich, J.; Unger, E.; Nickel, N. H. Building Blocks of Hybrid

- Perovskites: A Photoluminescence Study of Lead-Iodide Solution Species. *ChemPhysChem* **2020**, *21* (20), 2327–2333.
- (8) Jeon, N. J.; Noh, J. H.; Kim, Y. C.; Yang, W. S.; Ryu, S.; Seok, S. I. Solvent Engineering for High-Performance Inorganic–Organic Hybrid Perovskite Solar Cells. *Nat. Mater.* **2014**, *13* (9), 897–903.
- (9) Fei, C.; Li, B.; Zhang, R.; Fu, H.; Tian, J.; Cao, G. Highly Efficient and Stable Perovskite Solar Cells Based on Monolithically Grained CH<sub>3</sub>NH<sub>3</sub>PbI<sub>3</sub> Film. *Adv. Energy Mater.* **2017**, *7* (9), 1602017. <https://doi.org/10.1002/aenm.201602017>.
- (10) Zhang, H.; Nazeeruddin, M. K.; Choy, W. C. Perovskite Photovoltaics: The Significant Role of Ligands in Film Formation, Passivation, and Stability. *Adv. Mater.* **2019**, *31* (8), 1805702.
- (11) Chao, L.; Niu, T.; Gao, W.; Ran, C.; Song, L.; Chen, Y.; Huang, W. Solvent Engineering of the Precursor Solution toward Large-area Production of Perovskite Solar Cells. *Adv. Mater.* **2021**, *33* (14), 2005410.
- (12) Yang, M.; Li, Z.; Reese, M. O.; Reid, O. G.; Kim, D. H.; Siol, S.; Klein, T. R.; Yan, Y.; Berry, J. J.; van Hest, M. F. A. M.; Zhu, K. Perovskite Ink with Wide Processing Window for Scalable High-Efficiency Solar Cells. *Nat. Energy* **2017**, *2* (5), 17038. <https://doi.org/10.1038/nenergy.2017.38>.
- (13) Hamill Jr, J. C.; Schwartz, J.; Loo, Y.-L. Influence of Solvent Coordination on Hybrid Organic–Inorganic Perovskite Formation. *ACS Energy Lett.* **2017**, *3* (1), 92–97.
- (14) Yang, M.; Li, Z.; Reese, M. O.; Reid, O. G.; Kim, D. H.; Siol, S.; Klein, T. R.; Yan, Y.; Berry, J. J.; Van Hest, M. F. Perovskite Ink with Wide Processing Window for Scalable High-Efficiency Solar Cells. *Nat. Energy* **2017**, *2* (5), 1–9.
- (15) National Center for Biotechnology Information. “PubChem Compound Summary for CID 7964, Chlorobenzene.” *PubChem*.
- (16) Cataldo, F. A Revision of the Gutmann Donor Numbers of a Series of Phosphoramides Including TEPA. *Eur Chem Bull* **2015**, *4* (2), 92–97.
- (17) Abdelsamie, M.; Xu, J.; Bruening, K.; Tassone, C. J.; Steinrück, H.-G.; Toney, M. F. Impact of Processing on Structural and Compositional Evolution in Mixed Metal Halide Perovskites during Film Formation. *Adv. Funct. Mater.* **2020**, *30* (38), 2001752.
- (18) Babbe, F.; Sutter-Fella, C. M. Optical Absorption-based in Situ Characterization of Halide Perovskites. *Adv. Energy Mater.* **2020**, *10* (26), 1903587.
- (19) Qin, M.; Chan, P. F.; Lu, X. A Systematic Review of Metal Halide Perovskite Crystallization and Film Formation Mechanism Unveiled by in Situ GIWAXS. *Adv. Mater.* **2021**, *33* (51), 2105290.
- (20) Pratap, S.; Babbe, F.; Barchi, N. S.; Yuan, Z.; Luong, T.; Haber, Z.; Song, T.-B.; Slack, J. L.; Stan, C. V.; Tamura, N. Out-of-Equilibrium Processes in Crystallization of Organic-Inorganic Perovskites during Spin Coating. *Nat. Commun.* **2021**, *12* (1), 5624.
- (21) Szostak, R.; Sanchez, S.; Marchezi, P. E.; Marques, A. S.; Silva, J. C.; Holanda, M. S.; Hagfeldt, A.; Tolentino, H. C.; Nogueira, A. F. Revealing the Perovskite Film Formation Using the Gas Quenching Method by in Situ GIWAXS: Morphology, Properties, and Device Performance. *Adv. Funct. Mater.* **2021**, *31* (4), 2007473.
- (22) Suchan, K.; Just, J.; Becker, P.; Unger, E. L.; Unold, T. Optical in Situ Monitoring during the Synthesis of Halide Perovskite Solar Cells Reveals Formation Kinetics and Evolution of Optoelectronic Properties. *J. Mater. Chem. A* **2020**, *8* (20), 10439–10449.
- (23) Ono, L. K.; Juarez-Perez, E. J.; Qi, Y. Progress on Perovskite Materials and Solar Cells with



- Mixed Cations and Halide Anions. *ACS Appl. Mater. Interfaces* **2017**, *9* (36), 30197–30246.  
<https://doi.org/10.1021/acsami.7b06001>.
- (24) Petrov, A. A.; Sokolova, I. P.; Belich, N. A.; Peters, G. S.; Dorovatovskii, P. V.; Zubavichus, Y. V.; Khrustalev, V. N.; Petrov, A. V.; Grätzel, M.; Goodilin, E. A. Crystal Structure of DMF-Intermediate Phases Uncovers the Link between CH<sub>3</sub>NH<sub>3</sub>PbI<sub>3</sub> Morphology and Precursor Stoichiometry. *J. Phys. Chem. C* **2017**, *121* (38), 20739–20743.
- (25) Sharenko, A.; Mackeen, C.; Jewell, L.; Bridges, F.; Toney, M. F. Evolution of Iodoplumbate Complexes in Methylammonium Lead Iodide Perovskite Precursor Solutions. *Chem. Mater.* **2017**, *29* (3), 1315–1320.
- (26) Goldschmidt, V. M. Die Gesetze Der Krystallochemie. *Naturwissenschaften* **1926**, *14* (21), 477–485.
- (27) Li, Z.; Yang, M.; Park, J.-S.; Wei, S.-H.; Berry, J. J.; Zhu, K. Stabilizing Perovskite Structures by Tuning Tolerance Factor: Formation of Formamidinium and Cesium Lead Iodide Solid-State Alloys. *Chem. Mater.* **2016**, *28* (1), 284–292.
- (28) Li, J.; Dobrovolsky, A.; Merdasa, A.; Unger, E. L.; Scheblykin, I. G. Luminescent Intermediates and Humidity-Dependent Room-Temperature Conversion of the MAPbI<sub>3</sub> Perovskite Precursor. *ACS Omega* **2018**, *3* (10), 14494–14502.
- (29) Parrott, E. S.; Patel, J. B.; Haghghirad, A.-A.; Snaith, H. J.; Johnston, M. B.; Herz, L. M. Growth Modes and Quantum Confinement in Ultrathin Vapour-Deposited MAPbI<sub>3</sub> Films. *Nanoscale* **2019**, *11* (30), 14276–14284.
- (30) Protesescu, L.; Yakunin, S.; Bodnarchuk, M. I.; Krieg, F.; Caputo, R.; Hendon, C. H.; Yang, R. X.; Walsh, A.; Kovalenko, M. V. Nanocrystals of Cesium Lead Halide Perovskites (CsPbX<sub>3</sub>, X= Cl, Br, and I): Novel Optoelectronic Materials Showing Bright Emission with Wide Color Gamut. *Nano Lett.* **2015**, *15* (6), 3692–3696.
- (31) Lee, D.-K.; Shin, Y.; Jang, H. J.; Lee, J.-H.; Park, K.; Lee, W.; Yoo, S.; Lee, J. Y.; Kim, D.; Lee, J.-W.; Park, N.-G. Nanocrystalline Polymorphic Energy Funnel for Efficient and Stable Perovskite Light-Emitting Diodes. *ACS Energy Lett.* **2021**, *6* (5), 1821–1830.  
<https://doi.org/10.1021/acseenergylett.1c00565>.
- (32) Tian, W.; Leng, J.; Zhao, C.; Jin, S. Long-Distance Charge Carrier Funneling in Perovskite Nanowires Enabled by Built-in Halide Gradient. *J. Am. Chem. Soc.* **2017**, *139* (2), 579–582.  
<https://doi.org/10.1021/jacs.6b10512>.
- (33) Abdelsamie, M.; Li, T.; Babbe, F.; Xu, J.; Han, Q.; Blum, V.; Sutter-Fella, C. M.; Mitzi, D. B.; Toney, M. F. Mechanism of Additive-Assisted Room-Temperature Processing of Metal Halide Perovskite Thin Films. *ACS Appl. Mater. Interfaces* **2021**, *13* (11), 13212–13225.
- (34) Petrov, A. A.; Fateev, S. A.; Khrustalev, V. N.; Li, Y.; Dorovatovskii, P. V.; Zubavichus, Y. V.; Goodilin, E. A.; Tarasov, A. B. Formamidinium Haloplumbate Intermediates: The Missing Link in a Chain of Hybrid Perovskites Crystallization. *Chem. Mater.* **2020**, *32* (18), 7739–7745.  
<https://doi.org/10.1021/acs.chemmater.0c02156>.
- (35) Jiang, J.; Vicent-Luna, J. M.; Tao, S. The Role of Solvents in the Formation of Methylammonium Lead Triiodide Perovskite. *J. Energy Chem.* **2022**, *68*, 393–400.
- (36) Niu, T.; Chao, L.; Dong, X.; Fu, L.; Chen, Y. Phase-Pure  $\alpha$ -FAPbI<sub>3</sub> for Perovskite Solar Cells. *J. Phys. Chem. Lett.* **2022**, *13* (7), 1845–1854.

- (37) Huang, T.; Tan, S.; Nuryyeva, S.; Yavuz, I.; Babbe, F.; Zhao, Y.; Abdelsamie, M.; Weber, M. H.; Wang, R.; Houk, K. N. Performance-Limiting Formation Dynamics in Mixed-Halide Perovskites. *Sci. Adv.* **2021**, *7* (46), eabj1799.
- (38) Song, T.-B.; Yuan, Z.; Mori, M.; Motiwala, F.; Segev, G.; Masquelier, E.; Stan, C. V.; Slack, J. L.; Tamura, N.; Sutter-Fella, C. M. Revealing the Dynamics of Hybrid Metal Halide Perovskite Formation via Multimodal in Situ Probes. *Adv. Funct. Mater.* **2020**, *30* (6), 1908337.
- (39) Jacobsson, T. J.; Hultqvist, A.; García-Fernández, A.; Anand, A.; Al-Ashouri, A.; Hagfeldt, A.; Crovetto, A.; Abate, A.; Ricciardulli, A. G.; Vijayan, A. An Open-Access Database and Analysis Tool for Perovskite Solar Cells Based on the FAIR Data Principles. *Nat. Energy* **2022**, *7* (1), 107–115.
- (40) Hoye, R. L. Z.; Schulz, P.; Schelhas, L. T.; Holder, A. M.; Stone, K. H.; Perkins, J. D.; Vigil-Fowler, D.; Siol, S.; Scanlon, D. O.; Zakutayev, A.; Walsh, A.; Smith, I. C.; Melot, B. C.; Kurchin, R. C.; Wang, Y.; Shi, J.; Marques, F. C.; Berry, J. J.; Tumas, W.; Lany, S.; Stevanović, V.; Toney, M. F.; Buonassisi, T. Perovskite-Inspired Photovoltaic Materials: Toward Best Practices in Materials Characterization and Calculations. *Chem. Mater.* **2017**, *29* (5), 1964–1988.  
<https://doi.org/10.1021/acs.chemmater.6b03852>.
- (41) Kresse, G.; Joubert, D. From Ultrasoft Pseudopotentials to the Projector Augmented-Wave Method. *Phys. Rev. B* **1999**, *59* (3), 1758.
- (42) Kresse, G.; Hafner, J. Ab Initio Molecular Dynamics for Liquid Metals. *Phys. Rev. B* **1993**, *47* (1), 558.
- (43) Kresse, G.; Furthmüller, J. Efficiency of Ab-Initio Total Energy Calculations for Metals and Semiconductors Using a Plane-Wave Basis Set. *Comput. Mater. Sci.* **1996**, *6* (1), 15–50.
- (44) Perdew, J. P.; Burke, K.; Ernzerhof, M. Generalized Gradient Approximation Made Simple. *Phys. Rev. Lett.* **1996**, *77* (18), 3865.
- (45) Grimme, S.; Antony, J.; Ehrlich, S.; Krieg, H. A Consistent and Accurate Ab Initio Parametrization of Density Functional Dispersion Correction (DFT-D) for the 94 Elements H-Pu. *J. Chem. Phys.* **2010**, *132* (15), 154104.
- (46) Limas, N. G.; Manz, T. A. Introducing DDEC6 Atomic Population Analysis: Part 2. Computed Results for a Wide Range of Periodic and Nonperiodic Materials. *RSC Adv.* **2016**, *6* (51), 45727–45747.
- (47) Manz, T. A. Introducing DDEC6 Atomic Population Analysis: Part 3. Comprehensive Method to Compute Bond Orders. *RSC Adv.* **2017**, *7* (72), 45552–45581.
- (48) Li, N.; Tao, S.; Chen, Y.; Niu, X.; Onwudinanti, C. K.; Hu, C.; Qiu, Z.; Xu, Z.; Zheng, G.; Wang, L. Cation and Anion Immobilization through Chemical Bonding Enhancement with Fluorides for Stable Halide Perovskite Solar Cells. *Nat. Energy* **2019**, *4* (5), 408–415.
- (49) Li, Q.; Chen, Z.; Tranca, I.; Gaastra-Nedea, S.; Smeulders, D.; Tao, S. Compositional Effect on Water Adsorption on Metal Halide Perovskites. *Appl. Surf. Sci.* **2021**, *538*, 148058.
- (50) Li, Q.; Gaastra-Nedea, S.; Smeulders, D.; Tao, S. Accelerated Formation of Iodine Vacancies in CH<sub>3</sub>NH<sub>3</sub>PbI<sub>3</sub> Perovskites: The Impact of Oxygen and Charges. *EcoMat* **2022**, e12320.

## TOC

